A. Donizetti, T. Bellosta, A. Rausa, B. Re, A. Guardone
Level-Set Mass-Conservative Front-Tracking Technique for Multistep Simulations of In-Flight Ice Accretion
Journal of Aircraft, published online 01/02/2023
doi:10.2514/1.C037027

A Level-Set Mass-Conservative Front-Tracking Technique for Multi-Step Simulations of In-Flight Ice Accretion

Alessandro Donizetti*, Tommaso Bellosta,† Andrea Rausa,‡ Barbara Re,§ Alberto Guardone,¶
Department of Aerospace Science and Technology, Politecnico di Milano, Milano, Italy, 20156

This paper presents a novel level-set-based approach to model evolving boundary problems for in-flight ice accretion. No partial differential equations are solved as in the standard level-set formulation, but simple geometrical quantities are employed to provide an implicit discretization of the updated boundary. This method avoids mesh entanglements and grid intersections typical of algebraic and mesh deforming techniques, making it suitable for generating a body-fitted discretization of arbitrarily complex geometries as in-flight ice shapes, including the collision of separate ice fronts. Moreover, this paper presents a local ice thickness correction, which accounts for the body's curvature, to conserve the prescribed iced mass locally. The verification includes ice accretion over an ellipse and a manufactured example to show the proposed strategy's advantages and robustness compared to standard algebraic methods. Finally, the method is applied to ice accretion problems. A temporal and grid convergence study is presented for automatic multi-step in-flight simulations over a NACA0012 airfoil in rime, glaze, and mixed ice conditions.

I. Introduction

In-flight ice accretion is a critical issue in aeronautics since it can possibly cause significant degradation of aerodynamic performances and even more severe problems related to aircraft handling and control. A crucial aspect that characterizes and makes numerical simulations challenging is the formation, and evolution in time, of complex ice geometries, resulting from the ice accretion over the body surface and/or previously formed ice. Ice prediction software [1–4] generally handle this aspect through a quasi-steady, sequential approach that, starting from simulations of the flow field around the aircraft, predicts the trajectories of water droplets impinging on the surface and determines the amount of ice that accretes during the time interval over each boundary cell, be it a portion of the clean wing or the already iced geometry. Then, to advance the simulation in time, the computational mesh must be updated to capture the new position of the interface between air and ice, namely, the new geometry to be used in aerodynamic simulations.

*Ph.D. Candidate, Department of Aerospace Science and Technology, alessandro.donizetti@polimi.it
†Ph.D. Candidate, Department of Aerospace Science and Technology, tommaso.bellosta@polimi.it
‡Ph.D. Candidate, Department of Aerospace Science and Technology, andrea.rausa@polimi.it
§Assistant Professor, Department of Aerospace Science and Technology, barbara.re@polimi.it
¶Full Professor, Department of Aerospace Science and Technology, alberto.guardone@polimi.it

To this purpose, diverse approaches have been developed in the literature, depending on the grid topology employed for the computations. Indeed, either Body-Fitted Methods (BFM) or Immersed Boundary Methods (IBM) can be employed for such simulations. If a body-fitted mesh is employed for the CFD computations, the most straightforward approach to generating a new geometry is a simple grid deformation technique based on node displacement at fixed connectivity, following, for instance, the spring or the linear elasticity analogy. More robust mesh deformation strategies rely on a conservative, interpolation-free mesh adaptation technique to relocate the mesh nodes [5] or to change the grid connectivity within the arbitrary Lagrangian-Eulerian framework [6–8]. However, the motion of the ice-air interface results in a deformation that is usually local and non-smooth and could lead to intersections or non-physical regions in the updated geometry when dealing with concave regions or complex geometries such as ice shapes. Hence, standard mesh deformation techniques, generally developed for possible large but smooth deformations, cannot be straightforwardly applied to in-flight ice simulation, without the need of remeshing [2, 9].

In [10] is presented a robust strategy based on a structural frame analogy to avoid, or at least delay, the remeshing while preserving nearly orthogonal elements at the ice surface. Interpolation techniques that compute the displacement of all mesh nodes subjected to a given boundary displacement field solving an interpolation problem can be considered [11]. However, these schemes, which are transparent with respect to the grid connectivity, allow a limited displacement and require global and local smoothing techniques to preserve grid quality [9, 12]. Similarly, radial basis function (RBF) [13, 14] has been recently applied also to in-flight ice accretion problem [15, 16], but it seems unable to preserve a good quality mesh when dealing with complex geometries and large displacements. However, none of these methods could deal with the issue, common in multi-step ice accretion simulations, of mesh entanglement, depicted in Fig. 1. In the plot, the leading edge of a typical wind turbine airfoil (S 809) is superimposed on the ice shapes resulting from multi-step ice accretion. As the ice thickness increases, the interface geometry gets more complex, and the nodal displacement technique is not able to track or handle the intersection of the grid edges. Similar issues arise also in front collisions, that is when two or more ice fronts touch and merge together.

On the other side, IBMs circumvent the problem of precisely tracking the ice-air interface defining it as the zero contour surface of the level-set function [18]. This strategy was first applied to ice accretion simulations by Pena et at. [19]; later, it was used also in multi-layer simulations using B-spline curves to improve the interface representation [20]. A similar IBM strategy has been proposed also in [21]. Recently, Lavoie et al. [22] have compared the results of an IBM strategy and of a body-fitted strategy. These works show that IBMs are a promising strategy to deal with the complex geometries that may result from ice accretion, as they simplify the mesh generation and adaptation tasks. The level-set function is an Eulerian formulation of the evolution in time of a function ϕ in the domain and can be written in a non-conservative way as:

$$\frac{\partial \phi}{\partial t} + \mathbf{u} \cdot \nabla \phi = 0 \tag{1}$$

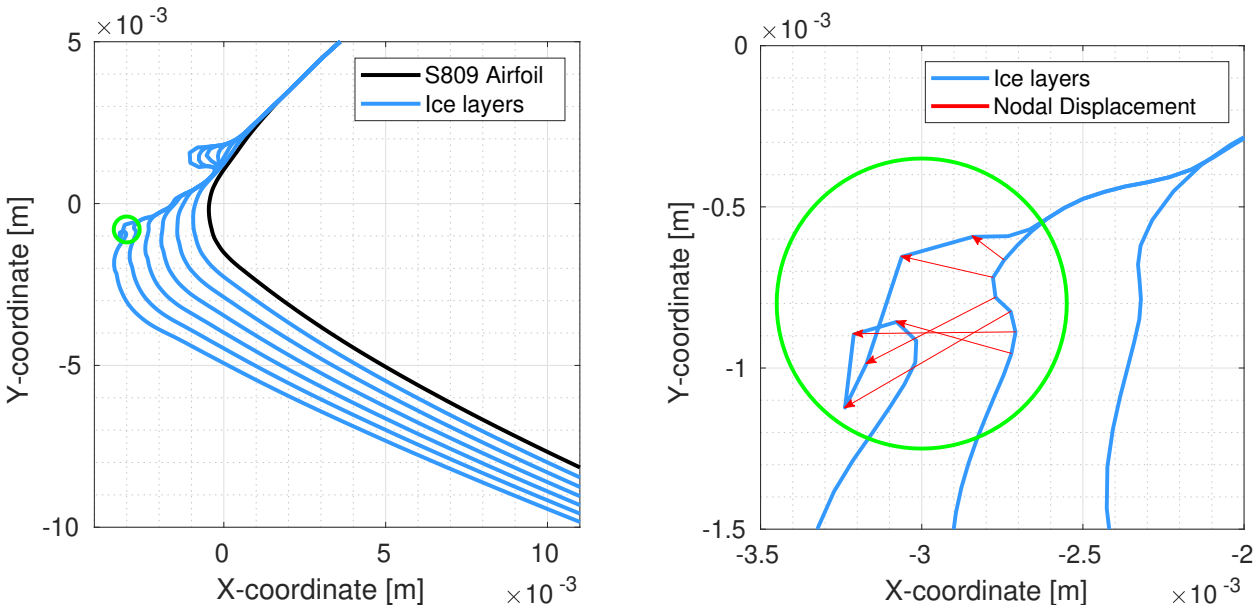

Fig. 1 Geometry entanglement in an ice accretion multi-step simulation, test conditions taken from [17].

where **u** is the velocity of the advancing front. In all mentioned IBMs, ϕ is the signed distance from the immersed boundary, that is the ice-air interface or the clean surface. However, imposing boundary conditions on such grids is a challenging task, and the accuracy of the solution near the boundaries is not easy to preserve [22]. Indeed, the computation of the aerodynamic flow field near ice horns and sharp features like trailing edges is often inaccurate, especially if compared with the solution obtained with the body-fitted approach. This inaccuracy can be critical in ice accretion simulations since the ice growth strongly depends on the shear stresses and the convective heat transfer at the wall.

In this work, the level-set formulation is originally combined with unstructured mesh adaptation techniques [23, 24] to profit from the advantages of both IBMs and BFMs. The proposed robust strategy is able to obtain a body-fitted mesh compliant with complex geometries and even front collisions. Instead of solving the hyperbolic advection equation for ϕ, two simple sets of information—the ice thickness to be accreted at the boundary and the distance of each grid node from the boundary—are combined to define the new body-fitted boundary discretization. Moreover, a local correction of the computed boundary displacement is enforced according to the boundary's curvature to conserve the total amount of prescribed material. Preliminary work in this context is presented in [25].

Considering a single-time step, given as inputs the computational grid and the volume of the material that accumulates over each boundary edge along its normal direction, the key steps of the proposed strategy are:

1) piecewise linear representation of the interface that enforces local conservation;
2) implicit definition of the interface through a level-set formulation, based on a signed distance field where the 0-level defines the interface;

3) mesh adaptation to describe the interface accurately;
4) extraction of the boundary discretization compliant with the updated position of the interface, to generate the new body-fitted mesh.

The last step leaves open the possibility of generating unstructured, structured, or hybrid meshes for the fluid domain.

This paper illustrates the interface tracking strategy over two-dimensional unstructured grids and validates it through multi-step simulations of ice accretion around airfoils, where the grid is generated automatically at every time step according to the new ice shape. For this purpose, the proposed strategy was integrated into PoliMIce [26], the computational toolkit for in-flight ice accretion problems under development at Politecnico di Milano.

Although applied here to ice accretion simulations, the proposed methodology can be adopted in any application that requires the deformation of a body-fitted mesh to conservatively account for the accumulation or erosion of a prescribed volume of material on the boundary. Examples include the erosion of thermal protection material in re-entry flights and material deposition in additive manufacturing. So, in the following, the ice accretion framework is used for validation and verification purposes without limiting the generality of the presented methodology.

The paper is structured as follows. In section II, the PoliMIce ice accretion software is described, including the implicit domain meshing strategy and the local thickness correction for mass conservation. In section III, the verification of the proposed approach is carried out for simple geometries. In section IV, the proposed method is applied to different ice accretion test cases including both rime and glaze ice conditions. In section V, final comments are given.

II. Methodology

In this section, the PoliMIce ice accretion software is firstly introduced to provide the general framework in which the novel interface tracking technique is inserted. The aerodynamic solver is presented in subsec. II.A, the particle tracking code for the computation of the collection efficiency is presented in subsec. II.B, and the ice accretion module is presented is subsec. II.C. Then, the novel strategy for the implicit representation of the iced boundary is illustrated in subsec. II.D, starting from a piecewise constant distribution of the ice thickness provided by the ice accretion module. Finally, in subsec. II.E, it is described how to compute a piecewise linear distribution of the thickness such that the total ice mass corresponds to the original one computed by the accretion module.

A. Aerodynamic solver

Aerodynamic simulation of the external airflow is performed here using SU2. The SU2 software suite [27] is an open-source toolkit written in C++ and Python created for multi-physics simulation and design. It is built specifically for solving partial differential equations (PDEs) and PDE-constrained optimization problems on unstructured meshes with state-of-the-art methods and algorithms. A node-centered finite volume method (FVM) is applied on arbitrary unstructured meshes using a standard edge-based data structure on a dual grid with median-dual control volumes.

Convective fluxes are discretized at each edge mid-point using either centered or upwind schemes. Discretization using upwind schemes can be coupled with a linear reconstruction via the MUSCL approach to yield a second-order scheme in space. Viscous fluxes are discretized using a corrected average of gradients approach. Source terms are approximated at each node using a piecewise constant reconstruction within each control volume. Gradients are obtained via a weighted least-squares approach. Regarding time integration, SU2 can solve implicitly steady and unsteady problems using a dual-time stepping strategy, leading to second-order accuracy and time. The core of the suite is a Reynolds-averaged Navier-Stokes (RANS) solver, which is used in this study in tandem with the Spalart–Allmaras (SA) [28] turbulence model.

B. Particle tracking module

The droplet solver aims to compute the collection efficiency β over the aircraft, which is used to compute the water mass collected at a given location on the surface. It involves the computation of the two-phase flow of water and air. Due to the scales at play in ice accretion and, in particular, the small diameter of the water droplets, their effects on the solution of the airflow field can usually be neglected so that the computation of the aerodynamics can be performed independently of the water droplets. This assumption leads to the so-called one-way coupled method; only the airflow field can affect the motion of water droplets. The in-house particle tracking code is based on a Lagrangian framework and it is used to simulate clouds containing supercooled water droplets [29]. The Lagrangian framework allows straightforward modeling of supercooled water droplets effects, such as splashing effects, aerodynamic breakup, and deformation, and can deal with secondary particles.

The cloud impinging the aircraft surfaces is represented as a single front initially placed at an arbitrary distance ahead of the aircraft. This distance is set so that droplets are traced starting from an unperturbed region of the domain and so that the computational burden related to the trajectory time integration, proportional to the integration length, is bearable. As the final result depends on the particle resolution, a strategy was developed to automatically refine the seeding region by adding new particles where needed. The seeding front, initially uniform, is discretized as a structured mesh of linear (in 2D) or quadrilateral (in 3D) elements. Elements are incrementally split at each iteration, evolving the current cloud front and computing the collection efficiency β on the surface. The simulation stops when the difference in the L_2 norm between two consecutive collection efficiency calculations is below a user-supplied threshold. In the present work, the chosen threshold is 10^{-6}. In practical applications, clouds are poly-dispersed. A standard approach deals with this problem by tracking a uniform cloud of droplets with a diameter equal to the Median Volume Diameter (MVD). That is the particle size that divides the total mass of the cloud in two. Half the mass comes from droplets of a diameter smaller than the cloud MVD, half from particles larger than the MVD. A more refined discretization of the particle size distribution can be considered by subdividing the droplets' size probability distribution function in a given number of bins. For each bin, a simulation can be performed, and the final collection efficiency can be obtained as a

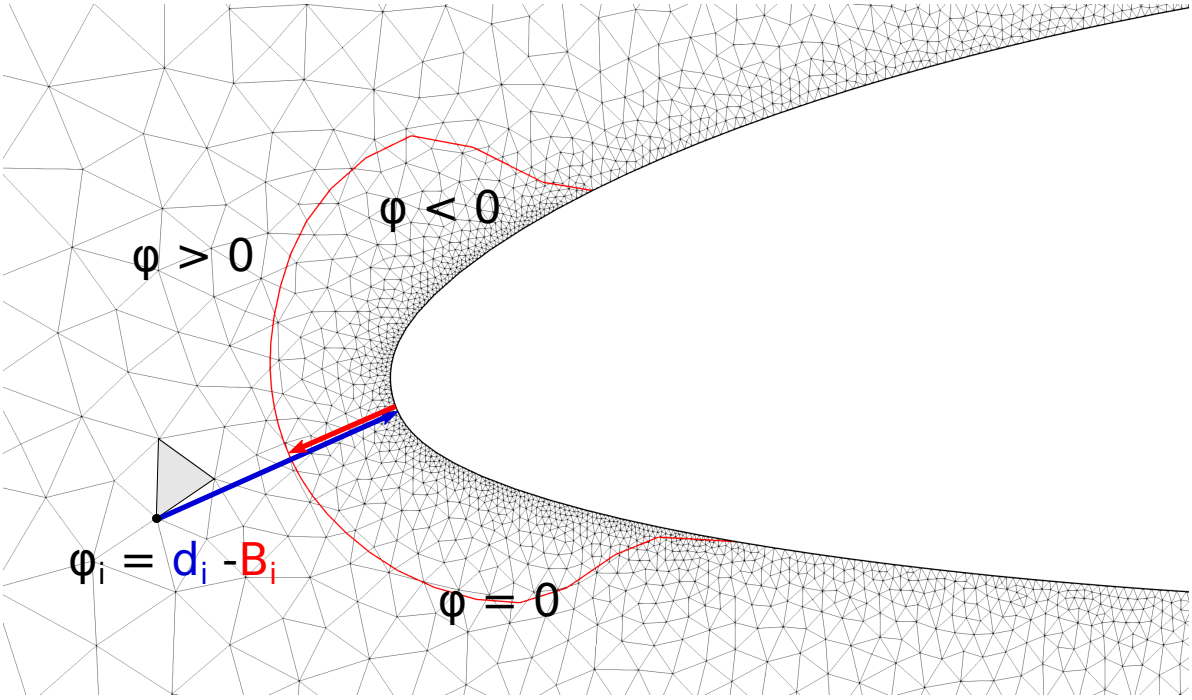

Fig. 2 Discrete definition of the level-set function over the simplicial computation domain.

weighted sum of the bins' β.

C. Ice accretion module

The in-house code PoliMIce [26] is used for computing the ice accretion. Computing the thickness of the accreting ice layer amounts to solving a phase change problem over the body surface. Typically surfaces are first discretized in computational cells, and a one-dimensional Stefan problem [30] is solved for each control volume. Most icing tools still rely on the first numerical formulation of the Stefan problem, proposed by Messinger in 1953 [31] for aeronautical applications. In 2001 Myers [32] proposed an improved version of Messinger's model, obtaining a better representation of the transition between the rime and the glaze ice. A further modification to Myers'model, based on the exact local solution of the unsteady Stefan problem, is implemented in the current version of PoliMIce [33]. It includes models for mass fluxes related to sublimation, allows mass transfer from rime to glaze cells, and introduces a new temperature profile, different from the linear one proposed by Myers to be consistent with the hypothesis of constant wall temperature. It is essential to underline that the ice accretion problem is assumed to be one-dimensional and that a piecewise constant representation of the solution is obtained over each cell.

D. Implicit interface discretization under the level set formulation

The level-set method is a general approach for the computation of moving curves and surfaces using an implicit formulation, originally proposed by Osher in 1988 [18]. Given a 2D domain $\Omega \subset \mathbb{R}^2$, a curve can be represented by a

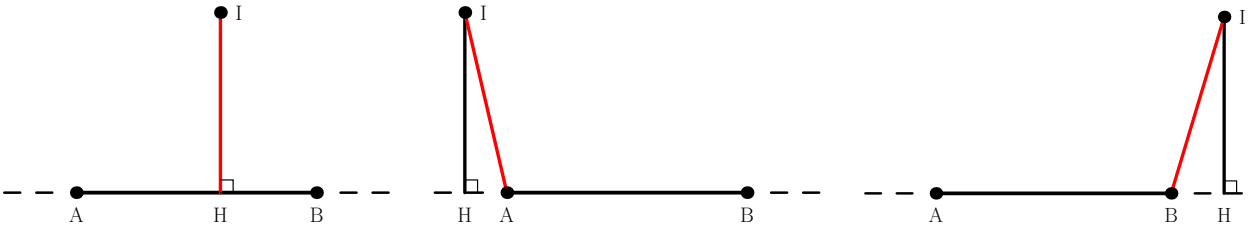

(a) Minimum distance is $\overline{\text{IH}}$ **(b) Minimum distance is $\overline{\text{IA}}$** **(c) Minimum distance is $\overline{\text{IB}}$**

Fig. 3 Minimum distance between the generic point I and a boundary segment delimited by vertices A and B.

certain level-set (or isocontour) of the auxiliary function $\phi(\mathbf{x}, t)$, with $\mathbf{x} \in \Omega$. Considering the accretion of material over the boundary of the computational domain otherwise empty, $\phi(\mathbf{x}, t)$ is an implicit function defined so that:

- $\phi(\mathbf{x}, t) < 0$ in the portion of the domain occupied by material,
- $\phi(\mathbf{x}, t) > 0$ in the portion of the domain not occupied by material,
- $\phi(\mathbf{x}, t) = 0$ at the interface.

Standard level-set approaches compute the evolution of the quantity $\phi(\mathbf{x}, t)$ by solving a Cauchy problem for the hyperbolic advection equation (1).

In contrast, the method suggested in the present work builds a discrete field that implicitly defines the interface location for the time considered. At each grid point i, the quantity $\phi_i = \phi(\mathbf{x}_i)$ is defined as

$$\phi_i = d_i - B_i\,, \qquad \text{with} \quad d_i = \left\|\mathbf{x}_i - \mathbf{x}_{i|B}\right\| \quad \text{and} \quad B_i = B(\mathbf{x}_{i|B}), \tag{2}$$

where $\mathbf{x}_{i|B}$ is the point on the solid boundary closest to $\mathbf{x}_i$, d_i is the distance of the point i from $\mathbf{x}_{i|B}$, and B_i is the prescribed amount of material for the point $\mathbf{x}_{i|B}$. The interface is represented over the domain by the reconstruction of the zero level solution of the scalar variable $\phi(\mathbf{x}, t)$. See Fig. 2 for an illustration, where the blue arrow represents the distance of a generic point from the solid boundary ($d_i = \left\|\mathbf{x}_i - \mathbf{x}_{i|B}\right\|$), while the red one indicates the prescribed material thickness on the closest boundary cell $B(\mathbf{x}_{i|B})$. The red line represents the air-ice interface target, obtained through a nodal displacement technique, corresponding to the zero level of $\phi(\mathbf{x}, t)$.

In 2D, calculating the distance d_i translates to computing the minimum distance between the considered point i and a list of edges that define the body, that is the boundary edges. Two cases can occur when computing the distance between a point and a segment (see Fig. 3):

- the foot of the projected distance (H) lies within the segment (Fig. 3a), or
- the foot of the projected distance (H) lies outside the limits of the segment (Fig. 3b and Fig. 3c).

In the first case, the minimum distance is the actual distance to the segment, while in the latter case it is the distance between the point H and the vertex of the segment closest to P. In this work, the values of the ice thickness are stored at the nodes representing the surface geometry, that is the airfoil surface at the beginning of the simulation, or the

interface at the previous time step. To obtain a continuous representation of the ice-air interface, the corresponding ice shape along each surface element is given by a linear interpolation between its nodal values. However, the output of PoliMIce is the ice thickness over each surface element, resulting only in a piecewise constant representation of the ice-air interface. Moving from a piecewise constant to a piecewise linear representation is to be done with care because of mass conservation. The computation of the nodal values starting from a piecewise constant material distribution is detailed in section II.E.

Once that the nodal values for the level set function $\phi(\mathbf{x})$ are defined over the discretized domain Ω_h, one needs to extract the zero level curve of $\phi(\mathbf{x})$. To accomplish this task, the implicit domain meshing implemented in the open-source library libmmg2d [34] was used. It can be summarized in the following three steps:

1) Each simplex element that is intersected by the zero level curve of the level-set function ϕ is marked, looking only at the relative signs of ϕ at the nodes of the considered element.
2) For each selected element, the edges intersected by the level-set are identified, and a new point is inserted along each edge in the correspondence of the zero level curve. In order to locate the new point, a linear interpolation is performed between the values at the nodes delimiting the edge. If from the splitting of a generic triangular element one obtains a triangular and a quadrilateral element, the latter is further locally split into two simplicial elements.
3) Finally, local mesh refinement is performed, swapping edges, and inserting, removing and relocating mesh vertices, to improve the overall mesh quality.

The reader is referred to [34] for the details of the implementation. Fig. 4 represents a typical output of the depicted implicit domain strategy. In particular, the portion of the domain occupied by ice is represented in blue, the portion of the domain occupied by air is represented in white, and the red line represents the air-ice interface target. At this point, one can extract separately each portion of the domain (for instance, in ice accretion problems, the part of the mesh with negative ϕ can be used to investigate heat transfer properties or ice cracking patterns for shedding [35]), as well as the set of edges connecting all points at $\phi = 0$ which represents the target ice-air interface at the new time step.

For a multi-step procedure, the points selected are sequentially reordered, e.g. starting from the trailing edge in a counter clockwise direction, and passed to the mesh generator Pointwise [36]. According to the needs of the aerodynamic solver, either structured, unstructured, or hybrid meshes can be generated. In this work, the aerodynamic flow field is computed with the Navier-Stokes solver of the open-source CFD solver SU2 [27], and thus hybrid body-fitted meshes are generated from the interface-compliant boundary discretization, to resolve accurately the boundary layer. Note that the mesh used for the implicit domain strategy does not necessarily coincide with the one used for the CFD computations.

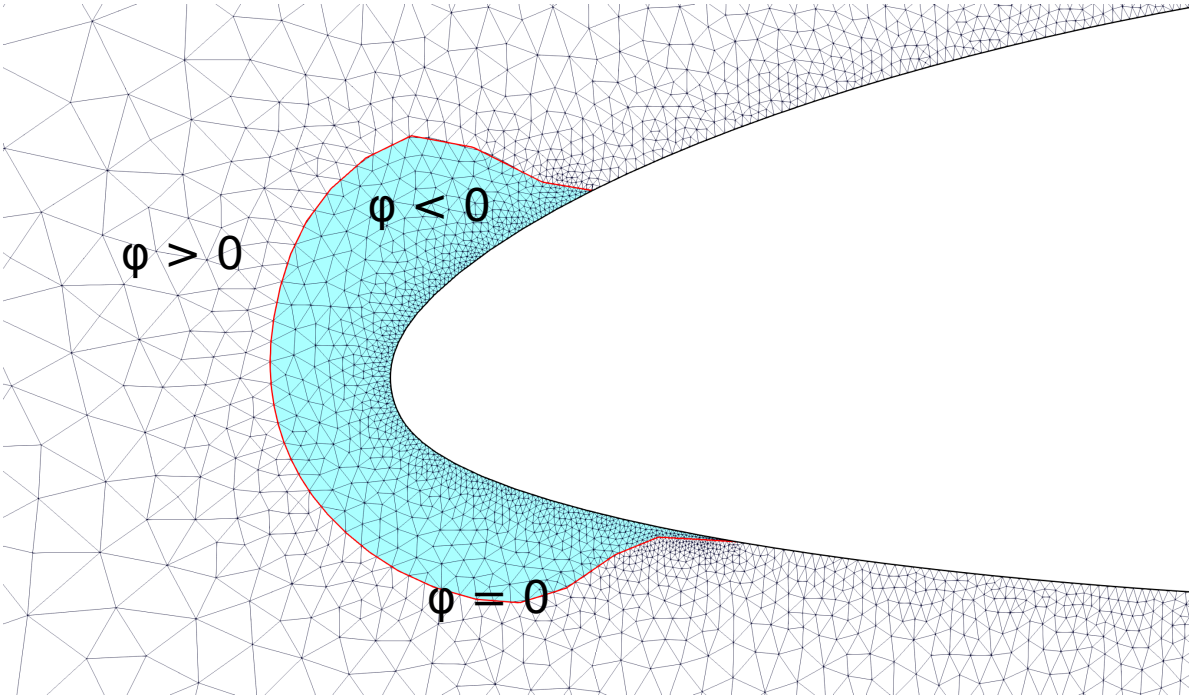

Fig. 4 Schematic representation of the implicit domain strategy adopted for the representation of the ice-air interface.

E. Local correction for mass conservation

A crucial aspect while simulating ice accretion is the conservation of the ice mass associated with each boundary element. Considering a constant density material, this is directly correlated to the conservation of the volume, or area in 2D. Within the present context, loss or gain of material can arise at different levels: during the extraction of points in the level-set formulation, during the new mesh generation process, or during the definition of the new nodal values to pass from the piecewise constant representation of the ice-air interface to the piecewise linear one. While the first and the second causes are strongly related to grid spacing and can be alleviated by smaller grid elements around the body, the third one is a much more delicate aspect, correlated to the body geometry, and it is addressed in this work.

Considering a discretized geometry, as a layer propagates perpendicularly to the surface, mimicking the physic of ice accretion, two things may occur: if the surface is convex, a gap is created at the vertex P (i.e. the dashed triangle formed by vertices P, P'_1, P'_2 in Fig. 5a); if the surface is concave, the two layers overlap (i.e. the dashed quadrilateral formed by vertices P, P'_1, P', P'_2 in Fig. 5b). This results, respectively, in a gain and in a loss of the accumulated mass with respect to the prescribed one. When defining the level-set function $\phi(\mathbf{x})$ according to eq. (2), the real shape obtained after the thickness propagation is taken into account to conserve the prescribed material mass locally. To compute the generic corrected nodal value $\widetilde{B}_i$, it is imposed the conservation of the area A_i, defined as half of the sum of the areas prescribed on the adjacent cells to node i. Fig. 6 displays the definition of the corrected thickness at the boundary point i, both for the convex and the concave case. In the former, once a value is assigned at the node, since the distance value

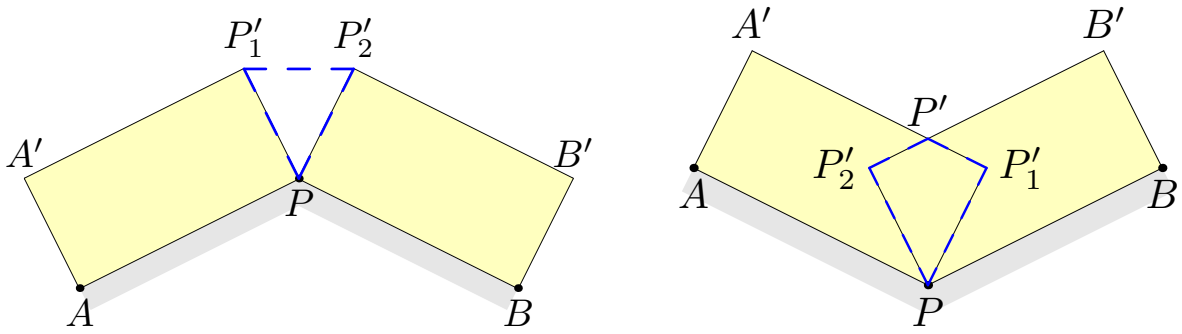

(a) Gain of material mass. **(b) Loss of material mass.**

Fig. 5 Schematic representation of the gain and loss of material due to the presence of curved, discretized, geometries. The apex indicates the updated position.

is not associated with any directional information, all the grid points within the circular sector of radius equal to the prescribed ice thickness $\widetilde{B}_i$ and angle α, having as a nearest neighbor the vertex node i, will have a negative value of the level-set function ϕ (which indicates a grid region occupied by ice).

To compute the value of $\widetilde{B}_i$, the resulting area (blue area in Fig. 6a) is expressed as function of the unknown thickness $\widetilde{B}_i$. By setting this area equal to the area A_i, the nodal value $\widetilde{B}_i$ that guarantees the local conservation of the mass prescribed on the adjacent cells can be computed as:

$$\widetilde{B}_{i_{\text{convex}}} = \frac{-(l_{j-1}+l_j) + \sqrt{(l_{j-1}+l_j)^2 + 2\alpha\left(l_{j-1}B_{j-1}+l_jB_j\right)}}{\alpha} \tag{3}$$

where l_j is the half of the length of the generic cell j and B_j is the prescribed ice thickness.

In the concave case, no gaps are formed, but there is instead a loss of area. To compensate it, an increased thickness value $\widetilde{B}_i$ is assigned to the node, keeping the sides of the resulting polygon (the short basis of the two trapezoids forming the red area in Fig. 6b) parallel to the walls. Again, to conserve mass locally, the sum of the red areas is set to be equal to A_i. This leads to:

$$\widetilde{B}_{i_{\text{concave}}} = \frac{(l_{j-1}+l_j) - \sqrt{(l_{j-1}+l_j)^2 - 4\frac{(l_{j-1}B_{j-1}+l_jB_j)}{\tan\beta}}}{\frac{2}{\tan\beta}} \tag{4}$$

Note that if different densities are prescribed on adjacent cells, as it occurs in icing simulations when different density models are employed [37], equations (3) and (4) must be modified accordingly. In particular, equation (3) can be rewritten as:

$$\widetilde{B}_{i_{\text{convex}}} = \frac{-(l_{j-1}\rho_{j-1}+l_j\rho_j) + \sqrt{(l_{j-1}\rho_{j-1}+l_j\rho_j)^2 + \alpha\left(\rho_{j-1}+\rho_j\right)\left(l_{j-1}B_{j-1}\rho_{j-1}+l_jB_j\rho_j\right)}}{\frac{\alpha(\rho_{j-1}+\rho_j)}{2}} \tag{5}$$

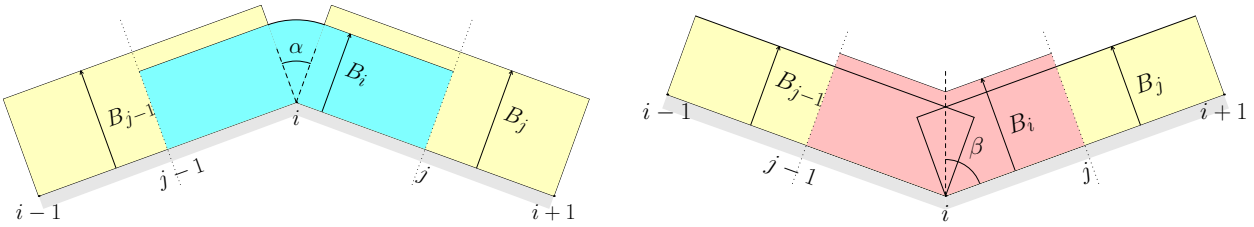

(a) Convex case. **(b) Concave case.**

Fig. 6 Local correction of the assigned thickness to a generic node for the convex (left) and concave case (right). Index i is used for nodes, while index j is used for edges.

and equation (4) as:

$$\widetilde{B}_{i_{\text{concave}}} = \frac{(l_{j-1}\rho_{j-1} + l_j\rho_j) - \sqrt{(l_{j-1}\rho_{j-1} + l_j\rho_j)^2 - 2\left(\rho_{j-1} + \rho_j\right)\frac{(l_{j-1}B_{j-1}\rho_{j-1} + l_j B_j\rho_j)}{\tan\beta}}}{\frac{(\rho_{j-1}+\rho_j)}{\tan\beta}} \tag{6}$$

So far, the conservative correction for a single boundary node has been discussed. If the correction is applied to the whole mesh, the resulting geometry is slightly different from the ones depicted in Fig. 6. When computing the implicit function ϕ_i at a generic grid point i, the material thickness value $\widetilde{B}_i$ is the result of the linear interpolation of the nodal values $\widetilde{B}_i$ at the boundary point closest to i; thus eq.(2) is replaced by

$$\phi_i = d_i - \Pi_{\tilde{B}}(\mathbf{x}_{i|B})\,, \tag{7}$$

where d_i and $\mathbf{x}_{i|B}$ are the same as in eq. (2), and $\Pi_{\tilde{B}}(\mathbf{x}_B)$ is the piecewise linear interpolation operator of the corrected thickness $\widetilde{B}$ over the boundary. An example of a possible resulting shape using the level-set function (7) is depicted in Fig. 7. The yellow area corresponds to the original prescribed thickness over each edge. The cyan and the red areas, for the convex and concave regions respectively, correspond to the locally modified thickness. The dashed blue line is the actual shape defined through the linear interpolation of the values stored at the nodes. In particular, the proposed strategy will cut the mesh exactly along this line.

It is crucial to notice that, in a convex-convex combination, mass conservation is still granted, which is no longer true when dealing with convex-concave or concave-concave combinations. However, the error introduced in these cases is negligible if the material thickness is not too large with respect to the length of the cells. There is still the possibility to retrieve the exact conservation of the prescribed mass by using a control point, see point $i - \frac{1}{2}$ in Fig. 7, at the midpoint of the generic cell, to allow another local thickness adjustment.

Another potential source of error stems from large concave angles between adjacent boundary edges associated with large material thickness, which would lead to a significant loss of mass due to the overlapping. The correction described by eq. (4) could transform the initial concavity into a spike. However, adding so much material to complex

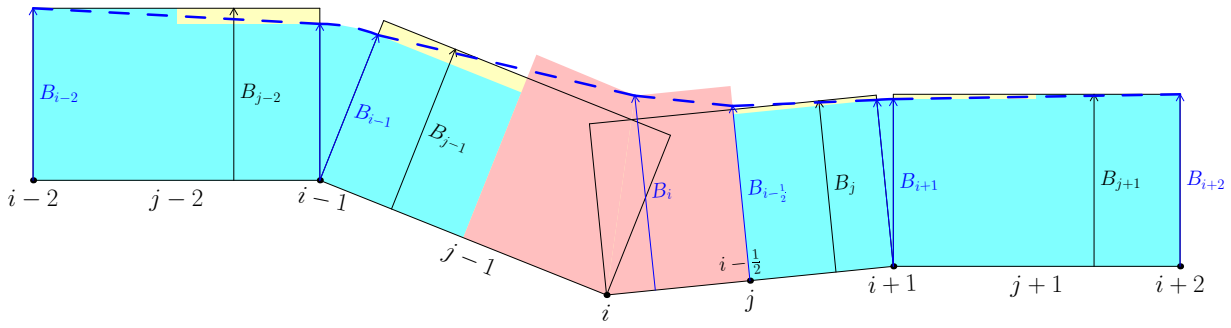

Fig. 7 Example of a reconstructed piecewise linear thickness distribution. Index i is used for nodes, while index j is used for edges.

geometries in a unique step is not recommended. In fact, the geometry would change during the accretion process, leading to entirely different final geometries.

III. Method Verification

In this section, three different accretion simulations are presented to highlight some distinctive capabilities of the proposed method. The first simulation is the accretion over a non-constant curvature body, which illustrates the importance of the corrections for mass conservation. The second one is the accretion over a manufactured geometry that shows the robustness of the proposed adaptive level-set method to track coalescing interfaces, which would lead to mesh tangling and geometry intersections if performed with nodal displacement techniques. The third one is a multi-step simulation of in-flight ice accretion, where at each step the geometry obtained through a nodal displacement technique is compared with the one obtained with the proposed methodology.

A. Uniform accretion over an ellipse

The first verification test is the uniform accretion over an ellipse of semi-axes $a = 6$ m and $b = 2$ m. In particular, once the ellipse is discretized with very fine elements, the same material thickness B is assigned to each element. In this example, $B = 1$ m. Let us call *constant thickness approach* the result obtained by moving each node perpendicularly to the surface of a quantity equal to the thickness B. The *mass conservative approach* instead considers the local thickness correction based on the surface curvature, as described in the previous section.

Both the *constant thickness approach* and the *mass conservative approach* are obtained using the level-set method. In the first case, simply no thickness correction is applied. Results are presented in Fig. 8.

Even if the analytical mass conservative solution for the continuous case is not available, the prescribed mass can be recovered by multiplying the thickness B by the approximated length of the ellipse L_e and by the arbitrary constant density $\rho = 1\,\mathrm{kg}/m^2$:

$$M = \rho \cdot B \cdot L_e = \rho \cdot B \cdot 4aE(e) \approx 26.7298 \text{ kg}$$

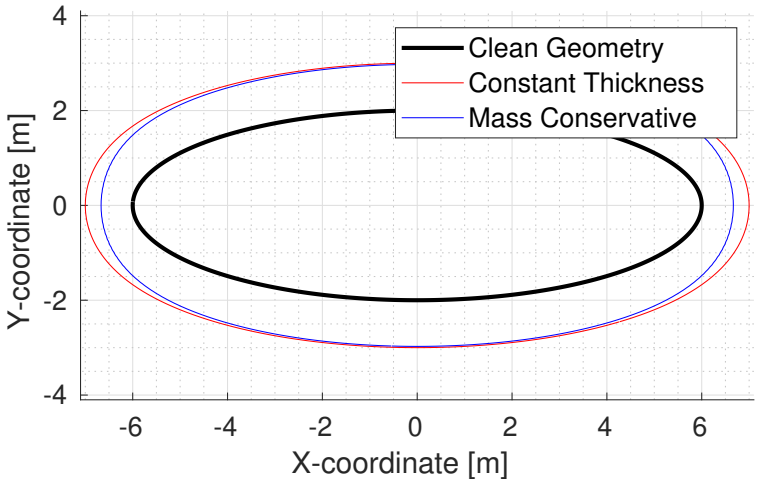

Fig. 8 Accretion of a uniformly distributed mass over a discretized ellipse. The result of the *constant thickness approach* is represented in red, while the result of the *mass conservative approach* is represented in blue.

where a is the semi-major axis, $E(k) = \int_0^{\pi/2} \sqrt{1 - k^2 \sin^2\theta}\, \mathrm{d}\theta$ is the complete elliptic integral of the second kind, and $e = \sqrt{1 - a^2/b^2}$ is the eccentricity of the ellipse. The relative mass error obtained with the constant thickness approach is 11.76%, while it is only 0.05% if the thickness correction is applied. As expected, the higher the curvature, the more evident the thickness correction. At the point of maximum curvature, the mass preserving thickness is only 66% of the prescribed original one. Neglecting these corrections in a real case of ice accretion would lead to very different ice shapes and geometries that would significantly alter the surrounding flow field and the trajectories of the water droplets, with a cascade effect on the final results in a multi-step simulation. It is remarkable that in ice accretion simulations the deposited mass is usually computed first from impingement and the ice model, and the ice thickness is then retrieved via the density model. This is a very delicate aspect in ice accretion simulations and a relevant source of uncertainty, especially in mixed ice conditions and/or 3D problems [37].

B. Merging of two advancing fronts

The robustness of the proposed method is now illustrated with a critical, manufactured example: the merging of two advancing ice fronts. The initial geometry of this test, displayed in Fig. 9a, is built by adding two ice-like horns on a symmetric NACA0012 airfoil, creating a concave region at the leading edge. Then, two intersecting cosine ice shapes, represented in red in Fig. 9a, are analytically prescribed in the upper part and lower part of this concave region. This is a standard situation where typical algebraic methods and mesh deforming techniques would fail, due to the interpenetration of the boundaries. Please note that, as a consequence of the merging of the ice fronts, an air bubble is formed, as depicted in Fig. 9b. The points forming the air bubble are automatically excluded from the list of points describing the updated interface, since, as mentioned in section II.D, the points are ordered starting from the trailing edge, and therefore no internal points are encountered within the loop. The starting manufactured geometry, the merging

of the ice horns, and the new, remeshed, geometry are presented in Fig. 9a, Fig. 9b, and Fig. 9c. The proposed technique successfully captures the front collision and produces a single ice front that can be used in the next step of a multi-step procedure.

C. Mesh entanglement in a multi-step simulation

In a typical multi-step simulation of in-flight ice accretion, as the geometry evolves in time, concave and irregular features of the ice shape could lead to an invalid mesh due to geometry entanglement, which is instead avoided by the implicit domain meshing formulation adopted in this paper. In figure 10, the solution obtained through a nodal displacement technique is represented in red, while the one obtained with the proposed methodology is represented in blue. The right picture is a zoomed view of the upper horn region, where the geometry overlapping occurs due to the presence of a concave region. The airfoil considered is a 72-inches NACA 23012. Freestream velocity is set to 100 $\mathrm{m/s}$, with an angle of attack of 2°. Static temperature and pressure are set respectively to 266 K and 92000 Pa. A median volume diameter (MVD) of 21 μm and a liquid water content (LWC) of 1.05 $\mathrm{g/m^3}$ complete the cloud definition. The total simulation time is 400 seconds, with inner time steps of 20 seconds. Numerical details of the different modules for the ice growth computation are discussed thoroughly in the next paragraph since the main objective of this section is just the comparison between the geometries reconstructed through the two different methods.

The solution obtained with the level-set formulation almost overlaps perfectly with the algebraic at each time step when the latter produces no mesh entanglement. Indeed, starting from the 11^{th} layer, concave regions near the growing horns lead to a mesh intersection, which would mean the end of the simulation and require the user intervention to adjust the geometry, if possible. Instead, the robustness of the proposed methodology allows the simulation to continue until the final time, despite the inherent complexity of the growing ice shape.

IV. Icing Simulations

This section presents three ice-accretion problems over a NACA0012 airfoil, representative of different icing conditions, such as rime ice, glaze ice, and an intermediate condition called mixed ice [38]. The proposed conservative level-set interface tracking strategy results are compared to the available numerical data by Bourgault-Côté et al. [39], which implements a standard level-set approach, and experimental data from Wright et al. [40]. Test conditions are reported in table 1. The input to the problem are the angle of attack (AoA), the freestream velocity, temperature and pressure, the liquid water content (LWC) of the cloud, i.e. the grams of water contained in a cubic meter of air, the droplet median volume diameter (MVD) and the total icing exposure time. The last column reports the relative error in the total amount of the ice mass accreted over the surface compared to the prescribed one.

To assess convergence, the simulations are performed with 20, 40, and 80 time steps, and using 3 different meshes. In particular, each mesh is characterized by the minimal boundary edge size h_{min} which discretizes the leading edge. The

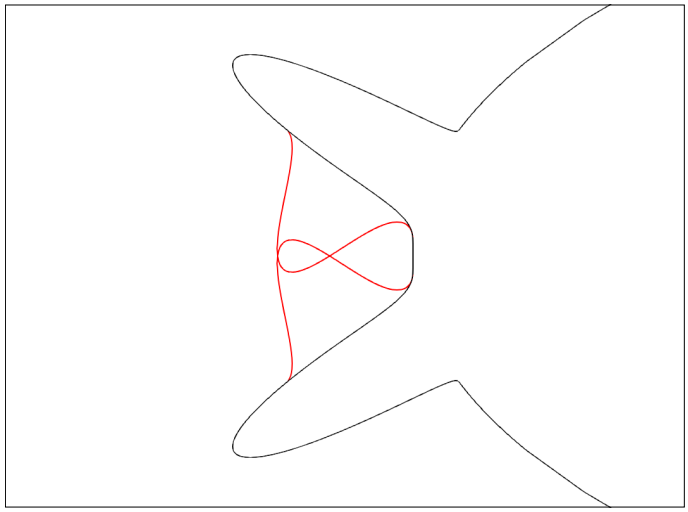

(a) Initial manufactured geometry. The black line represents the manufactured airfoil surface; the red line represents the prescribed ice shape, characterized by the intersections of the two fronts.

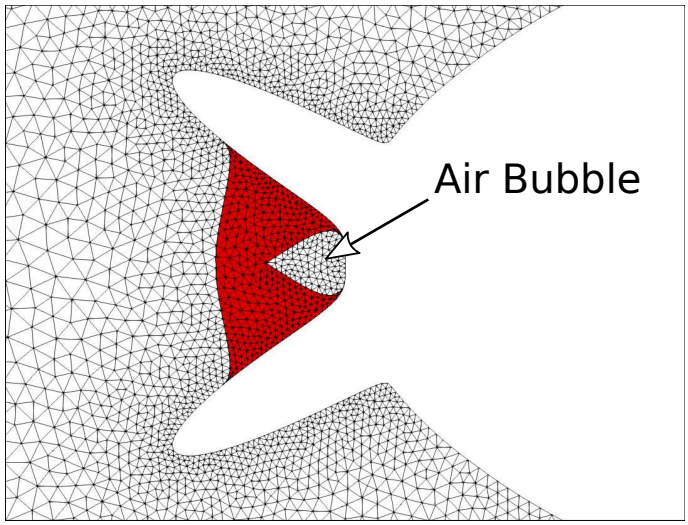

(b) Detail of the merging of two ice horns and the consequent formation of an air-bubble. The red region is the one occupied by the ice, the white region by air.

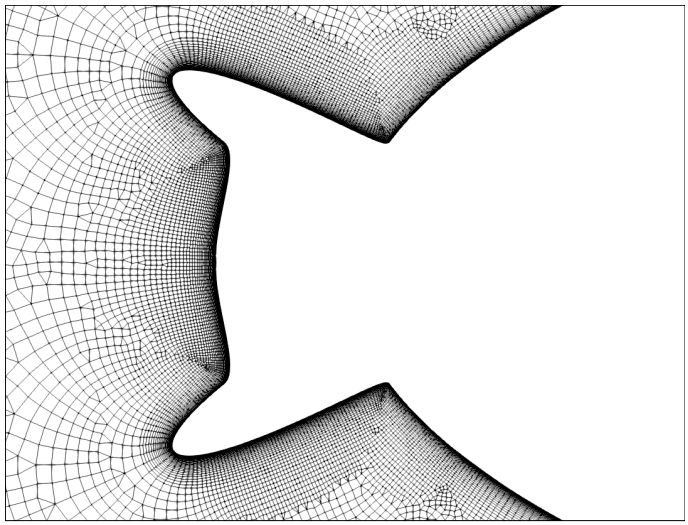

(c) Body-fitted mesh compliant with the updated geometry. The hybrid mesh is generated considering the final ice-air interface as solid boundary.

Fig. 9 Merging and subsequent remeshing of two advancing fronts.

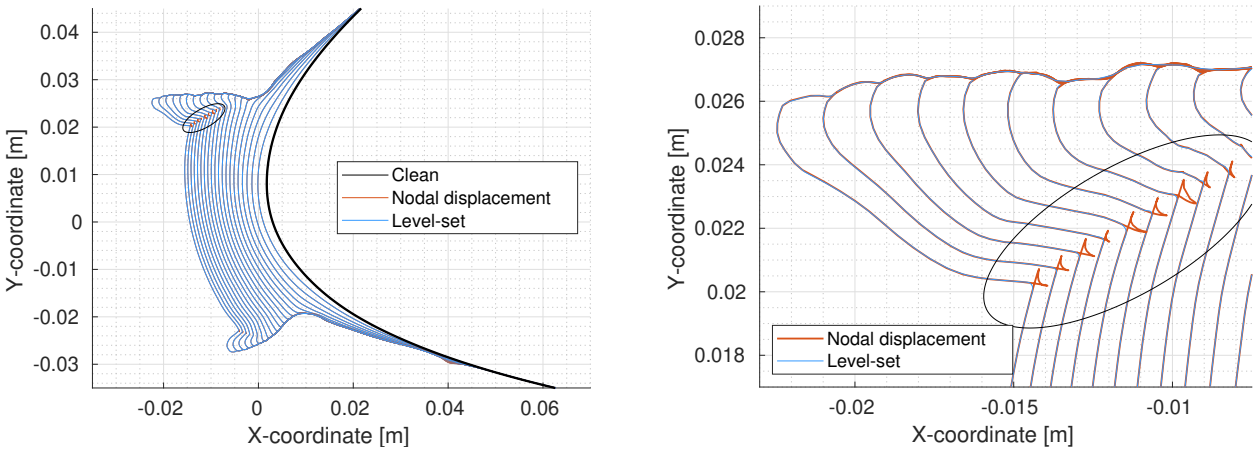

Fig. 10 Comparison between the solution obtained through a nodal displacement technique and the proposed level-set method.

coarse grid is characterized by $h_{min}/c = 0.003$, the medium grid by $h_{min}/c = 0.002$ and the fine grid by $h_{min}/c = 0.001$, where c is the airfoil chord. Each mesh is an hybrid mesh made of both quadrilateral and triangular elements. The boundary layer region is represented by a structured boundary layer to ensure $y^+ < 1$ everywhere and orthogonal elements.

The numerical methods for computing the flow field in SU2 are as follows. Roe's second-order upwind scheme is used to calculate the convective fluxes. Venkatakrishnan's limiter is applied to the primitive variables. Turbulent variables for the SA model are convected using a first-order scalar upwind method. The gradients of the variables are computed using a weighted least-squares method. An adaptive CFL is used for convergence acceleration. The numerical techniques and parameters for computing the collection efficiency are now introduced. A forward Euler integration scheme is used to integrate the particle trajectories with an integration time step of 10^{-5} s. A cloud of initially 1000 supercooled water droplets is progressively refined until two successive values of the L_2 norm of the collection efficiency β fall below the threshold of 10^{-6}. The cloud is located at approximately three chord lengths upstream of the airfoil. The cloud of supercooled water droplets is tracked in the computational domain until all particles have impacted with the airfoil and the collection efficiency is computed.

Multi step ice accretion is performed for these test cases, subdividing the total exposure time in equally smaller time

Table 1 Icing test conditions.

Test	AoA [°]	Velocity [m/s]	Temp [K]	Pressure [kPa]	LWC [g/m^3]	MVD [μm]	Icing Time [s]	Mass Err [%]
Rime Ice	4.0	93.89	242.5	92.06	1.05	20	372	0.96
Glaze ice	4.0	58.10	266.3	95.61	1.30	20	480	0.85
Mixed ice	4.0	93.89	260.8	92.06	1.05	20	372	0.70

intervals. To perform a sensitivity analysis, different time intervals have been tested. The model used in these test cases to help capture the complex experimental ice shapes is the local exact solution of the unsteady Stefan problem for the temperature profiles within the ice layer in glaze conditions [33]. The local surface temperature is used for the heat exchange. A steady liquid film model is used with an integration time step of 1 s. The rime and glaze ice density are respectively 880 $\mathrm{kg\,m^{-3}}$ and 917 $\mathrm{kg\,m^{-3}}$. However, no roughness model is applied to the ice shape [41–43]. Finally, it is computed the relative difference between the ice mass obtained after the level-set method and the one prescribed by PoliMIce. The errors are computed for the simulations with the highest number of time steps and the finest surface discretization. As reported in table 1, all the cases present a total mass error below 1%.

A. Rime Ice

With temperatures well below the freezing point, the rime ice is characterized by all the water freezing upon impingement, leading to the formation of relatively streamlined ice shapes. Both the time step and the mesh discretization analysis, illustrated in Fig. 11, suggest a convergence of the ice shape.

A comparison between the different ice shapes obtained with the highest number of time steps over the different mesh discretizations is presented in Fig. 11a, while the dependence on the number of time steps for each single mesh discretization is shown from Fig. 11b to Fig. 11d. In this test, all the spatial and temporal discretizations give similar results. For instance, the point where the ice starts to accrete and the maximum ice thickness are almost identical among the different simulations, and they fit reasonably well with the experimental data, despite a slight underestimation of the ice thickness in the nose region. The proposed technique is capable of reproducing the growth over time of these simple shapes.

B. Glaze Ice

The glace ice simulation is characterized by a higher static temperature and a higher liquid water content, with a lower free stream velocity. In particular, the relatively high temperature allows the water runback behaviour after the impinging point, leading to the formation of glaze ice, characterized by a more complex shape.

The results for the different grids and time steps are shown in Fig. 12. The total thickness of the ice shape computed in the central region, i.e., close to the leading edge of the airfoil, is the same in each simulation and accurately matches the experimental data. However, in all simulations, the lower part of the ice shape does not precisely fit the experimental data. This is probably due to the water runback behaviour, which PoliMIce does not capture. In particular, water droplets tend to freeze immediately upon the impingement instead of going further downstream.

The time step sensitivity, illustrated in Fig. 12b to 12d, suggests convergence for each of the meshes considered. On the contrary, as shown in Fig. 12a, there is a significant dependence on the dimension of the elements adopted for the airfoil discretization. In particular, the adoption of finer elements results in a change of the slope of the predicted

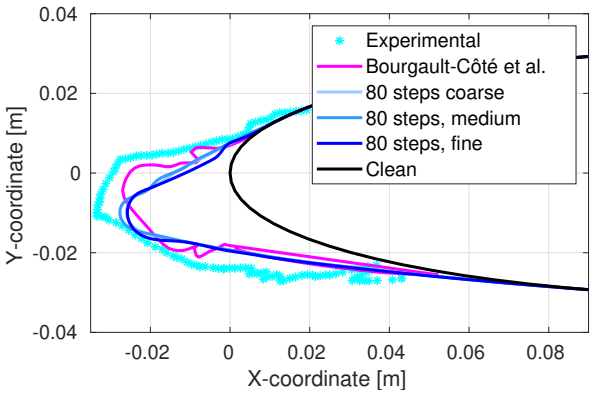

(a) Comparison between the final layers computed with 80 time steps over 3 different mesh discretizations.

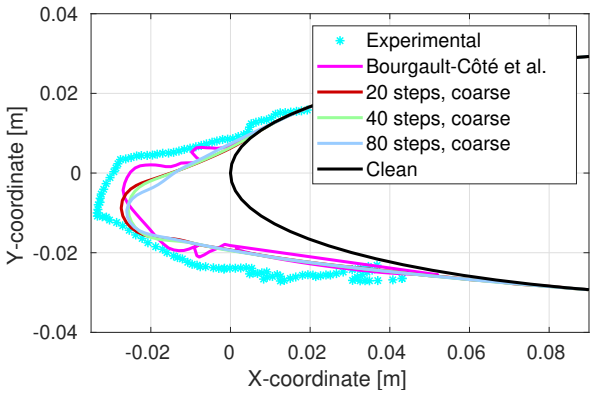

(b) Comparison between the final layers computed with different time steps over the coarse grid.

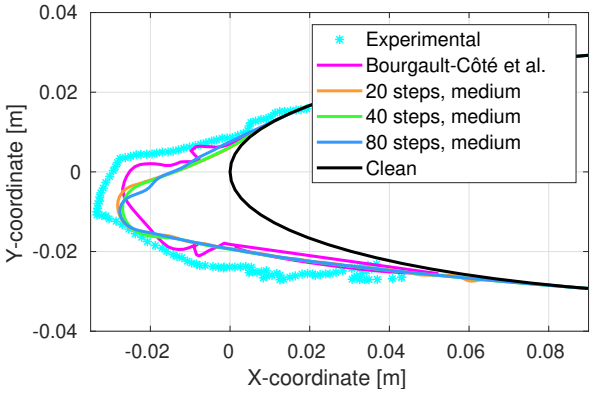

(c) Comparison between the final layers computed with different time steps over the medium grid.

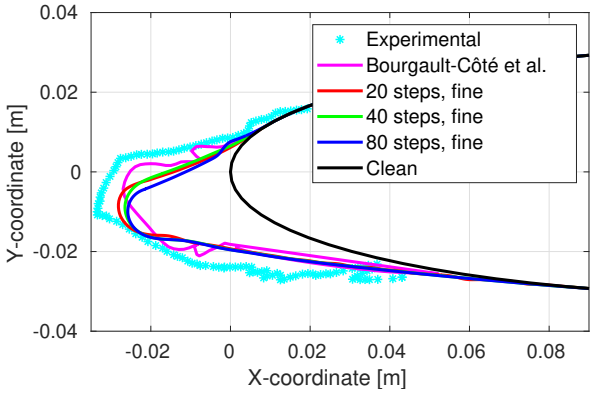

(d) Comparison between the final layers computed with different time steps over the fine grid.

Fig. 11 Rime Ice over a NACA 0012 airfoil. Numerical results obtained with the proposed level-set approach and the PoliMIce suite are compared to the experimental data from Wright et al. [40] and numerical data by Bourgault-Côté et al. [39]

upper horn considerably. At first glance, the coarser mesh seems to predict accurately the experimental ice shape. Nevertheless, the slope obtained with the fine grid is closer to the experimental one; simply, the upper ice accretion limit is slightly downward in the numerical results than in the experimental ones. This behavior could also suggest that the thermodynamic model used in PoliMIce, in particular the part describing the runback water, is not particularly suited to these test conditions.

C. Mixed Ice

The mixed ice case is characterized again by runback water, but only in the stagnation point region. In fact, the maximum thickness is not located at the leading edge but in the upper horn region. Differently from the previous cases, two notable horns develop here, making the simulation very challenging to be performed with standard techniques. The thickness predicted in the stagnation, and upper horn region is in good agreement with the experimental data, but,

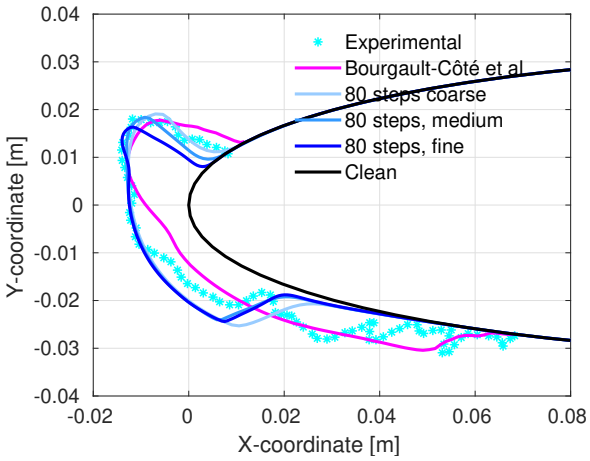

(a) Comparison between the final layers computed with 80 time steps over 3 different mesh discretizations.

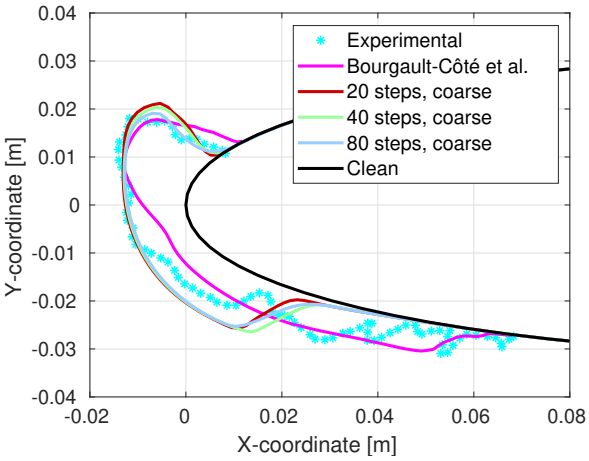

(b) Comparison between the final layers computed with different time steps over the coarse grid.

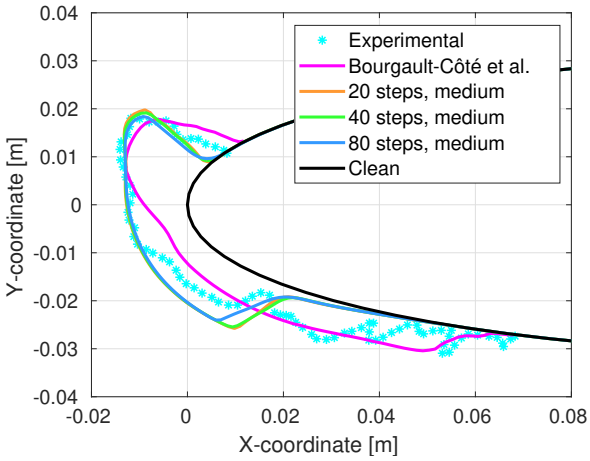

(c) Comparison between the final layers computed with different time steps over the medium grid.

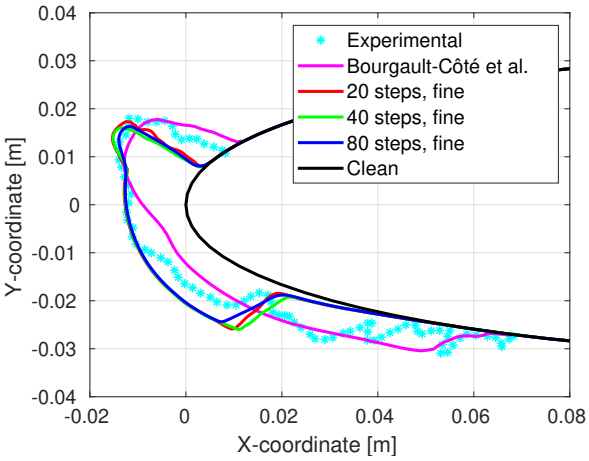

(d) Comparison between the final layers computed with different time steps over the fine grid.

Fig. 12 Glaze Ice over a NACA 0012 airfoil. Numerical results obtained with the proposed level-set approach and the PoliMIce suite are compared to the experimental data from Wright et al. [40] and numerical data by Bourgault-Côté et al. [39]

analogously to what was found for the glaze ice, there is an underestimation of the thickness of both the ice layer and the horn in the lower side.

The time step sensitivity analysis, illustrated in Fig. 13b to 13d, suggests convergence for each of the meshes considered. The mesh spacing sensitivity of the upper horn is instead significant, see Fig. 13a, as expected from such a complex ice geometry, while the lower horn is less affected by the grid discretization.

V. Conlusion

Within the context of ice accretion simulation, this paper proposed a new level-set-based strategy to accurately track the dynamic air-ice interface, which is implicitly defined by a discrete signed-distance field over an unstructured mesh.

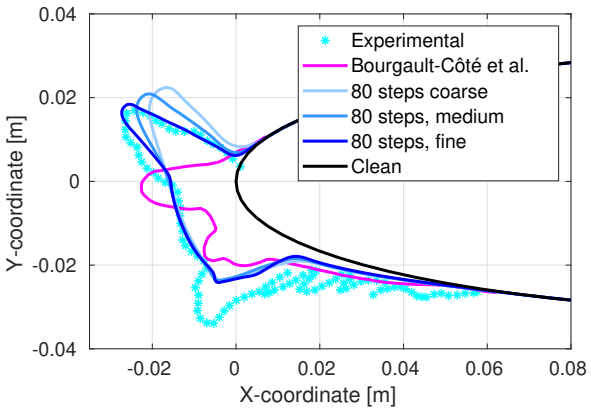

(a) Comparison between the final layers computed with 80 time steps over 3 different mesh discretizations.

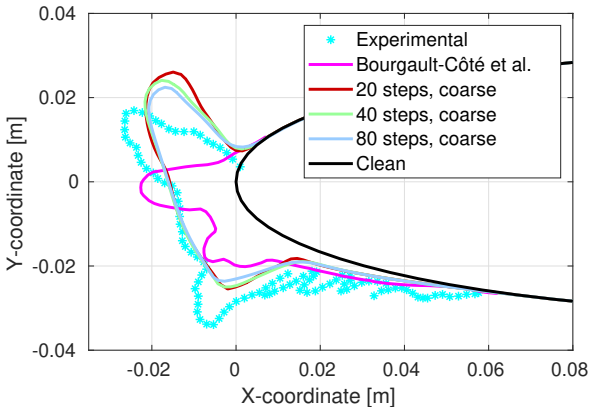

(b) Comparison between the final layers computed with different time steps over the coarse grid.

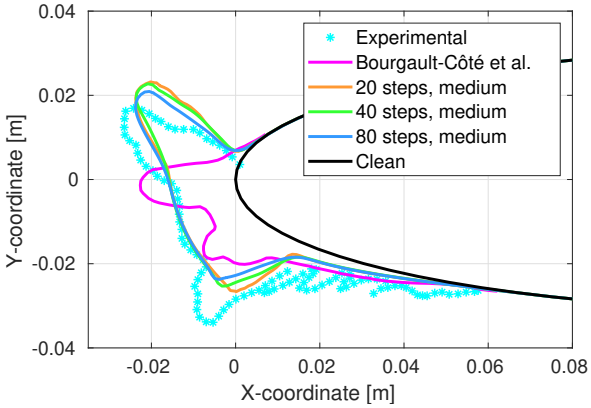

(c) Comparison between the final layers computed with different time steps over the medium grid.

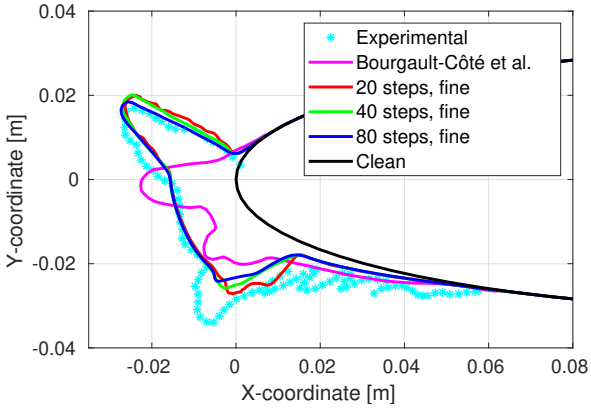

(d) Comparison between the final layers computed with different time steps over the fine grid.

Fig. 13 Mixed Ice over a NACA 0012 airfoil. Numerical results obtained with the proposed level-set approach and the PoliMIce suite are compared to the experimental data from Wright et al. [40] and numerical data by Bourgault-Côté et al. [39]

The proposed method does not suffer geometry updating limitations typical of standard algebraic methods, like nodal displacement techniques. Among the notable features, this strategy can locally conserve the prescribed amount of material to be accreted over the boundary. A time-step and mesh sensitivity analysis of the ice shape was conducted for three relevant ice accretion cases, namely, rime, glaze, and mixed ice accretion. Despite a very good convergence regarding temporal discretization, the authors have detected a crucial dependence on the size of the elements adopted to discretize the airfoil, which will be addressed in future studies.

The robustness of this strategy is important to assess the reliability of in-flight ice accretion simulations. Indeed, once mesh convergence is obtained, it is possible to properly investigate different modeling aspects of the thermodynamic module and include roughness models to establish their impact in multi-step simulations. Given its robustness, the proposed method can be applied to simulate long exposure times and precisely track arbitrarily complex interfaces, given that they are manifold solutions and an appropriately refined mesh is employed. In this regard, the smoothness of

the ice shapes, which may seem like a specific feature of the proposed strategy, is actually due to the choice of the ice accretion model.

Although conceived and validated in the context of ice accretion over aerodynamic surfaces, the proposed strategy is standalone, and it could be successfully exploited in different applications involving the accumulation or ablation of a given amount of material over a solid boundary. Finally, the proposed methodology shows great potential for 3D applications since the formation of cavities and scallops often results in front collisions and mesh entanglement and thus requires highly robust methods to be handled. The method presented here, which has proven to be able to avoid mesh entanglement and front collision, is, in the authors' opinion, a first move towards multi-step 3D simulations of ice accretion problems. Indeed, the extension of the proposed strategy to the 3D case is currently underway. Moreover, the proposed strategy to combine a level-set implicit definition of the interface and mesh adaptation techniques to generate a new body-fitted mesh can be easily generalized to 3D. Once that the nodal values of the level-set function are assigned to the points of a simplicial 3D volume, the tetrahedra can be split analogously to what happens for the triangles in 2D. For this specific task, the open-source library libmmg3d can be used, which has the same structure of its 2D counterpart. Currently, the major open issue in 3D is related to the mass conservation problem, since convex, concave, and even saddle points can be present in 3D. So, a correction to locally conserve mass also in 3D is currently under investigation. Once the answer is found, all the ingredients will be available to extend the proposed strategy to the 3D case.

Funding Sources

The ICE GENESIS project has received funding from the European Union's Horizon 2020 research and innovation program under grant agreement no. 824310.

References

[1] Wright, W. B., "User's Manual for LEWICE Version 3.2," Tech. Rep. NAS3-00145, National Aeronautics and Space Administration, Glenn Research Center, Cleveland, Ohio 44135, 1 November 2008.

[2] Beaugendre, H., Morency, F., and Habashi, W. G., "FENSAP-ICE's three-dimensional in-flight ice accretion module: ICE3D," *Journal of Aircraft*, Vol. 40, No. 2, 2003, pp. 239–247. https://doi.org/10.2514/2.3113.

[3] Saeed, F., Gouttebroze, S., and Paraschivoiu, I., "Modified canice for improved prediction of airfoil ice accretion," *8th Aerodynamic Symposium of 48th CASI Conference, Toronto, Canada, Apr*, Vol. 29, 2001, pp. 283–289.

[4] Radenac, E., "Validation of a 3D ice accretion tool on swept wings of the SUNSET2 program," *8th AIAA Atmospheric and Space Environments Conference*, 2016, p. 3735. https://doi.org/10.2514/6.2016-3735.

[5] Cirrottola, L., Ricchiuto, M., Froehly, A., Re, B., Guardone, A., and Quaranta, G., "Adaptive deformation of 3D unstructured meshes with curved body fitted boundaries with application to unsteady compressible flows," *Journal of Computational Physics*, Vol. 433, 2021, p. 110177. https://doi.org/10.1016/j.jcp.2021.110177.

[6] Colombo, S., and Re, B., "An ALE residual distribution scheme for the unsteady Euler equations over triangular grids with local mesh adaptation," *Computers & Fluids*, Vol. 239, 2022, p. 105414. https://doi.org/10.1016/j.compfluid.2022.105414.

[7] Re, B., Dobrzynski, C., and Guardone, A., "An interpolation-free ALE scheme for unsteady inviscid flows computations with large boundary displacements over three-dimensional adaptive grids," *Journal of Computational Physics*, Vol. 340, 2017, pp. 26–54. https://doi.org/10.1016/j.jcp.2017.03.034.

[8] Fossati, M., Khurram, R., and Habashi, W., "An ALE mesh movement scheme for long-term in-flight ice accretion," *International Journal for Numerical Methods in Fluids*, Vol. 68, No. 8, 2012, pp. 958–976. https://doi.org/10.1002/fld.2588.

[9] Tong, X., Thompson, D., Arnoldus, Q., Collins, E., and Luke, E., "Three-Dimensional Surface Evolution and Mesh Deformation for Aircraft Icing Applications," *Journal of Aircraft*, Vol. 54, No. 3, 2017, pp. 1047–1063. https://doi.org/10.2514/1.C033949.

[10] Pendenza, A., Habashi, W. G., and Fossati, M., "A 3D mesh deformation technique for irregular in-flight ice accretion," *International Journal for Numerical Methods in Fluids*, Vol. 79, No. 5, 2015, pp. 215–242. https://doi.org/10.1002/fld.4049.

[11] Luke, E., Collins, E., and Blades, E., "A fast mesh deformation method using explicit interpolation," *Journal of Computational Physics*, Vol. 231, No. 2, 2012, pp. 586–601. https://doi.org/10.1016/j.jcp.2011.09.021.

[12] Thompson, D. S., Tong, X., Arnoldus, Q., Collins, E., Luke, E. A., and Bidwell, C. S., "Discrete Surface Evolution and Mesh Deformation for Aircraft Icing Applications," *5th AIAA Atmospheric and Space Environments Conference*, American Institute of Aeronautics and Astronautics, Reston, Virginia, 2013, pp. 1–19. https://doi.org/10.2514/6.2013-2544.

[13] De Boer, A., Van der Schoot, M. S., and Bijl, H., "Mesh deformation based on radial basis function interpolation," *Computers & structures*, Vol. 85, No. 11-14, 2007, pp. 784–795. https://doi.org/10.1016/j.compstruc.2007.01.013.

[14] Rendall, T. C., and Allen, C. B., "Efficient mesh motion using radial basis functions with data reduction algorithms," *Journal of Computational Physics*, Vol. 228, No. 17, 2009, pp. 6231–6249. https://doi.org/10.1016/j.jcp.2009.05.013.

[15] Groth, C., Costa, E., and Biancolini, M. E., "RBF-based mesh morphing approach to perform icing simulations in the aviation sector," *Aircraft Engineering and Aerospace Technology*, Vol. 91, No. 4, 2019, pp. 620–633. https://doi.org/10.1108/AEAT-07-2018-0178.

[16] Morelli, M., Bellosta, T., and Guardone, A., "Efficient radial basis function mesh deformation methods for aircraft icing," *Journal of Computational and Applied Mathematics*, Vol. 392, 2021, p. 113492. https://doi.org/10.1016/j.cam.2021.113492.

[17] Han, Y., Palacios, J., and Schmitz, S., "Scaled ice accretion experiments on a rotating wind turbine blade," *Journal of Wind Engineering and Industrial Aerodynamics*, Vol. 109, 2012, pp. 55–67. https://doi.org/10.1016/j.jweia.2012.06.001, URL http://dx.doi.org/10.1016/j.jweia.2012.06.001.

[18] Osher, S., and Fedkiw, R., *Level set methods and dynamic implicit surfaces*, Springer Science & Business Media, 2006. https://doi.org/10.1007/b98879.

[19] Pena, D., Hoarau, Y., and Laurendeau, E., "A single step ice accretion model using Level-Set method," *Journal of Fluids and Structures*, Vol. 65, 2016, pp. 278–294. https://doi.org/10.1016/j.jfluidstructs.2016.06.001.

[20] Bourgault-Côté, S., Docampo-Sánchez, J., and Laurendeau, E., "Multilayer Airfoil Ice Accretion Simulations Using a Level-Set Method with B-Spline Representation," *AIAA Journal*, Vol. 57, No. 8, 2019, pp. 3299–3308. https://doi.org/10.2514/1.J057905.

[21] Al-Kebsi, A., Mose, R., and Hoarau, Y., "Multi-Step Ice Accretion Simulation Using The Level-Set Method," *EUCASS 2019, 8th European Conference for Aeronautics and Space Sciences*, 2019, pp. 1–13. https://doi.org/10.4271/2019-01-1955.

[22] Lavoie, P., Radenac, E., Blanchard, G., Laurendeau, E., and Villedieu, P., "An Immersed Boundary Method for Multi-Step Ice Accretion using a Level-Set," *AIAA Aviation Forum*, 2021, pp. 1–20. https://doi.org/10.2514/6.2021-2630.

[23] Re, B., Guardone, A., and Dobrzynski, C., "An Adaptive Conservative ALE Approach to Deal with Large Boundary Displacements in Three-Dimensional Inviscid Simulations," *55th AIAA Aerospace Sciences Meeting*, American Institute of Aeronautics and Astronautics, 2017, pp. 1–13. https://doi.org/10.2514/6.2017-1945, aIAA 2017-1945.

[24] Re, B., and Guardone, A., "An adaptive ALE scheme for non-ideal compressible fluid dynamics over dynamic unstructured meshes," *Shock Waves*, Vol. 29, 2019, pp. 73–99. https://doi.org/10.1007/s00193-018-0840-2.

[25] Donizetti, A., Re, B., and Guardone, A., "A level-set based mesh adaptation technique for mass conservative ice accretion in unsteady simulations," *9th International Conference on Computational Methods for Coupled Problems in Science and Engineering, COUPLED PROBLEMS 2021*, CIMNE, 2021, pp. 1–11. https://doi.org/10.23967/coupled.2021.004.

[26] Gori, G., Zocca, M., Garabelli, M., Guardone, A., and Quaranta, G., "PoliMIce: A simulation framework for three-dimensional ice accretion," *Applied Mathematics and Computation*, Vol. 267, 2015, pp. 96–107. https://doi.org/10.1016/j.amc.2015.05.081.

[27] Economon, T. D., and Palacios, F., and Copeland, S. R., and Lukaczyk, T. W., and Alonso, J. J., "SU2: An Open-Source Suite for Multiphysics Simulation and Design," *AIAA Journal*, Vol. 54, No. 3, 2015, pp. 828–846. https://doi.org/10.2514/1.J053813.

[28] Spalart, P., and Allmaras, S., "A One-Equation Turbulence Model for Aerodynamic Flows," *AIAA*, Vol. 439, 1992. https://doi.org/10.2514/6.1992-439.

[29] Bellosta, T., Parma, G., and Guardone, A., "A robust 3D particle tracking solver for in-flight ice accretion using arbitrary precision arithmetic," *8th International Conference on Computational Methods for Coupled Problems in Science and Engineering, COUPLED PROBLEMS 2019*, CIMNE, 2021, pp. 622–633.

[30] Stefan, J., "Ueber die Theorie der Eisbildung, insbesondere über die Eisbildung im Polarmeere," *Annalen der Physik*, Vol. 278, No. 2, 1891, pp. 269–286. https://doi.org/10.1002/andp.18912780206.

[31] Messinger, B., "Equilibrium Temperature of an Unheated Icing Surface as a Function of Air Speed," *Journal of the Aeronautical Sciences*, Vol. 20, 1953, pp. 29–42. https://doi.org/10.2514/8.2520.

[32] Myers, T., "Extension to the Messinger model for aircraft icing," *AIAA Journal*, Vol. 39, 2001, pp. 211–218. https://doi.org/10.2514/3.14720.

[33] Gori, G., Parma, G., Zocca, M., and Guardone, A., "Local Solution to the Unsteady Stefan Problem for In-Flight Ice Accretion Modeling," *Journal of Aircraft*, Vol. 55, No. 1, 2018, pp. 251–262. https://doi.org/10.2514/1.C034412.

[34] Dapogny, C., Dobrzynski, C., and Frey, P., "Three-dimensional adaptive domain remeshing, implicit domain meshing, and applications to free and moving boundary problems," *Journal of Computational Physics*, Vol. 262, 2014, pp. 358–378. https://doi.org/10.1016/j.jcp.2014.01.005.

[35] Rausa, A., Morelli, M., and Guardone, A., "A novel method for robust and efficient prediction of ice shedding from rotorcraft blades," *Journal of Computational and Applied Mathematics*, Vol. 391, 2021, p. 113452. https://doi.org/10.1016/j.cam.2021.113452.

[36] "Pointwise, Inc." https://www.pointwise.com/, 2007.

[37] Bidwell, C. S., "Icing Analysis of a Swept NACA 0012 Wing Using LEWICE3D Version 3.48," *6th AIAA Atmospheric and Space Environments Conference*, 2014, p. 2200. https://doi.org/10.2514/6.2014-2200.

[38] Gent, R., Dart, N., and Cansdale, J., "Aircraft icing," *Philosophical Transactions of the Royal Society A: Mathematical, Physical and Engineering Sciences*, Vol. 358, No. 1776, 2000, pp. 2873–2911. https://doi.org/10.1098/rsta.2000.0689.

[39] Bourgault-Cote, S., Docampo-Sánchez, J., and Laurendeau, E., "Multi-Layer Ice Accretion Simulations Using a Level-Set Method With B-Spline Representation," *2018 AIAA Aerospace Sciences Meeting*, 2018, pp. 1–13. https://doi.org/10.2514/6.2018-1835.

[40] Wright, W., Gent, R., and Guffond, D., "DRA/NASA/ONERA collaboration on icing research. Part 2; Prediction of airfoil ice accretion," Tech. rep., NASA, May 1997.

[41] McClain, S. T., Vargas, M. M., Tsao, J.-C., and Broeren, A. P., "A Model for Ice Accretion Roughness Evolution and Spatial Variations," *AIAA Aviation Forum*, 2021, p. 2641. https://doi.org/10.2514/6.2021-2641.

[42] Fortin, G., Laforte, J.-L., and Ilinca, A., "Heat and mass transfer during ice accretion on aircraft wings with an improved roughness model," *International Journal of Thermal Sciences*, Vol. 45, No. 6, 2006, pp. 595–606. https://doi.org/10.1016/j.ijthermalsci.2005.07.006.

[43] Han, Y., and Palacios, J., "Surface roughness and heat transfer improved predictions for aircraft ice-accretion modeling," *AIAA Journal*, Vol. 55, No. 4, 2017, pp. 1318–1331. https://doi.org/10.2514/1.J055217.